The mechanics of tip growth morphogenesis: what we have learned from rubber balloons

Permanent link

http://nrs.harvard.edu/urn-3:HUL.InstRepos:35427773

Share Your Story

The Harvard community has made this article openly available.
Please share how this access benefits you. Submit a story .

Accessibility

Journal of
Mechanics of
Materials and Structures

THE MECHANICS OF TIP GROWTH MORPHOGENESIS: WHAT
WE HAVE LEARNED FROM RUBBER BALLOONS

Roberto Bernal, Enrique R. Rojas and Jacques Dumais

THE MECHANICS OF TIP GROWTH MORPHOGENESIS: WHAT WE HAVE LEARNED FROM RUBBER BALLOONS

ROBERTO BERNAL, ENRIQUE R. ROJAS AND JACQUES DUMAIS

If you can't demonstrate it with balloons, it's probably not important anyway.

Stephen A. Wainwright, quoted in [Vogel 2003].

Morphogenesis of plant, fungal, and bacterial cells depends heavily on surface mechanics and in particular on the stiff wall that surrounds these cells. In this paper, we show that tubular rubber balloons offer a useful physical model of tip growth morphogenesis. In particular, the balloons reproduce accurately the inhomogeneity and anisotropy of surface expansion observed during tip growth. Comparison between the two systems has led to a simple model of tip growth that assumes linear constitutive relations with inhomogeneous material properties. The strain rate profile predicted by the model is a surprisingly good fit to the data given the model's simplicity. We suggest that a meridional gradient of compliance or extensibility is the key mechanical feature that explains the similar strain rate profiles in tip-growing cells across broad taxonomic groups as well as in rubber balloon analogs.

1. Introduction

Cells come in a variety of shapes that are often finely adapted to fulfill specific functions. A familiar example is the human red blood cell whose flexible biconcave geometry allows it to squeeze through narrow capillaries. The morphogenetic mechanisms that control the development of shape appear to be quite diverse [Harold 1990] and few are particularly well understood.

In bacteria, fungi, and plants, cell shape is to a large extent determined by the stiff extracellular matrix or cell wall surrounding the cell. The cell wall is a thin layer of polysaccharides and proteins assembled outside the plasma membrane. The architecture of cell walls can vary greatly although it typically takes the form of a fiber-reinforced composite where fibrils of cellulose (in plants) provide stiffness to the wall while an amorphous matrix of pectins helps maintain the cohesion between the different wall components.

This paper focuses on one important mode of cell morphogenesis called tip growth. The shape of tip-growing cells is characterized by a long cylinder capped by a prolate dome (Figure 1). Kinematics studies using cell surface markers have established that wall expansion is limited to the tip of the cell [Reinhardt 1892; Hejnowicz et al. 1977; Shaw et al. 2000; Dumais et al. 2004]. Expansion at the tip is maintained by two complementary processes: the addition of cell surface material and the mechanical deformation of the cell surface into the characteristic cylindrical shape. Vesicle exocytosis and polysaccharide synthesis
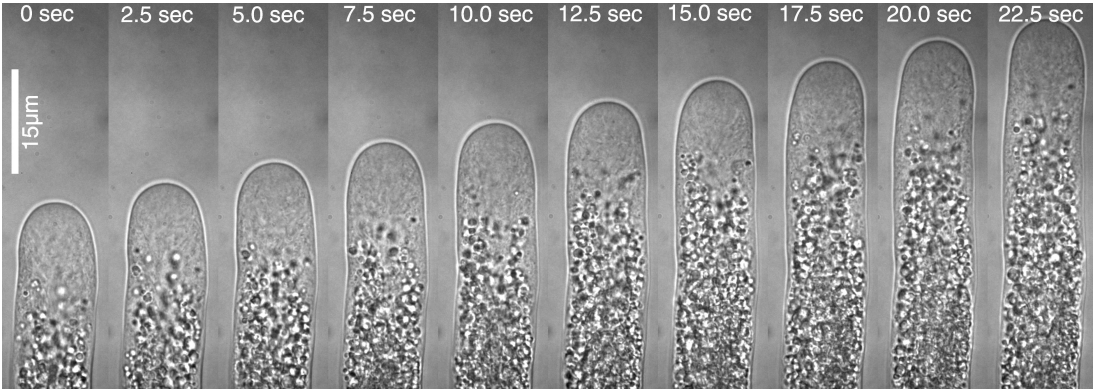
Figure 1. Tip growth morphogenesis of a lily pollen tube.

at the plasma membrane provide the material necessary to expand the surface. However, secretion of building material does not expand the cell surface unless the material is subsequently deformed and integrated into the preexisting extracellular matrix. This step requires mechanical work provided by the internal hydrostatic pressure of the cell.

Although models of tip growth are available, few have attempted an explicit comparison with the kinematics of these cells. The goal of this paper is to introduce a simple mechanical model that reproduces the key features of tip growth morphogenesis.

2. The kinematics of tip growth

Over a period of minutes or hours, the elongation of tip-growing cells is surprisingly steady both in terms of geometry and the rate of elongation, as shown in Figure 1 [Shaw et al. 2000]. Kinematics studies of tip growth have been performed using time-lapse imaging of marked cells [Castle 1958; Chen 1973; Hejnowicz et al. 1977; Shaw et al. 2000; Dumais et al. 2004]; see Figures 2 and 3. Given the axisymmetric geometry of these cells, two variables are sufficient to describe the entire morphogenetic
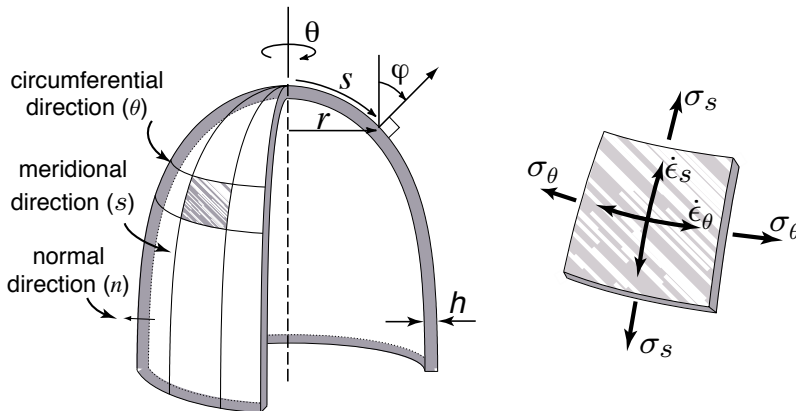

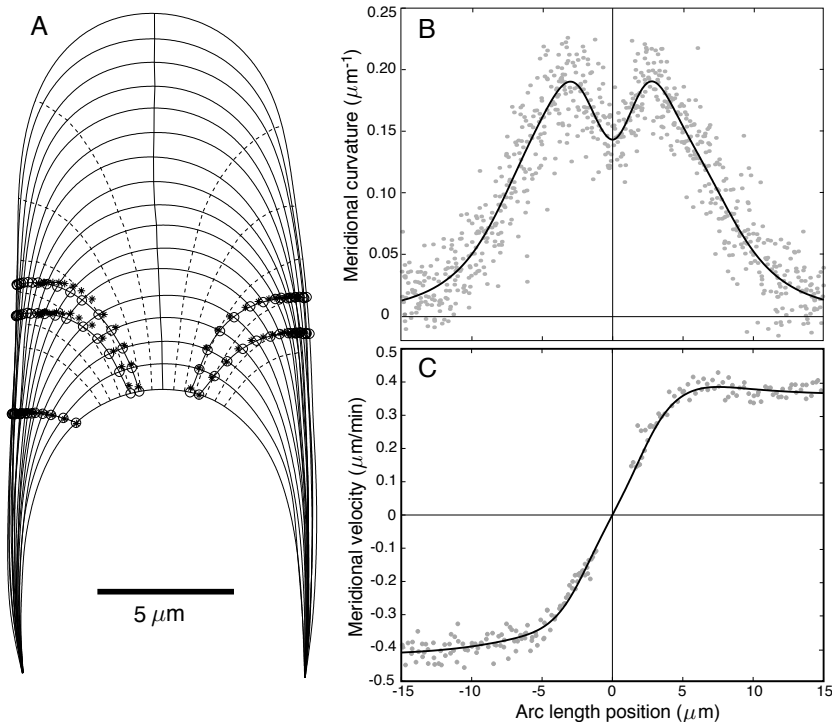**Figure 2.** Key geometrical variables for the description of tip growth.

Figure 3. Growth kinematics of a *Medicago truncatula* root hair. (A) The cell outline captured at a 3 min time interval. The displacement of five surface markers is shown (circles). The dotted lines indicate trajectories that are normal to the cell surface. (B) The meridional curvature of the cell. (C) The meridional velocity of material points. Modified from [Dumais et al. 2004].

process. The cell geometry is given by the meridional curvature (κ_s) (Figure 3B) while the rates of surface expansion can be derived from the meridional velocity (v) of material points with respect to the pole of the cell (Figure 3C). Given these variables, the strain rates are defined as [Hejnowicz et al. 1977; Dumais et al. 2004]:

$$\dot{\epsilon}_s = \frac{d}{ds}\frac{ds}{dt} = \frac{dv}{ds}, \qquad \dot{\epsilon}_\theta = \frac{1}{r}\frac{dr}{dt} = \frac{1}{r}\frac{dr}{ds}v, \tag{1}$$

where the variables are illustrated in Figure 2.

Studies of cellular tip growth have revealed two fundamental features of wall expansion: surface expansion is inhomogeneous and anisotropic (Figure 4). The inhomogeneity is seen in the sharp decline of the strain rates from a maximal value near the pole of the cell to zero on the side of the cell. Surface expansion also shows a characteristic anisotropy with meridional anisotropy ($\dot{\epsilon}_s > \dot{\epsilon}_\theta$) within two to three microns of the pole and extensive circumferential anisotropy ($\dot{\epsilon}_\theta > \dot{\epsilon}_s$) on the flanks of the tip (Figure 4).

The strain profile observed in root hairs is similar to those reported for other tip-growing cells including the *Chara* rhizoid [Hejnowicz et al. 1977], the *Nitella* rhizoid [Chen 1973], and the sporangiophore of *Phycomyces* [Castle 1958]. Since these systems include representatives of fungi, plants and algae, that differ greatly in wall chemistry and cell biology, one is tempted to attribute the similarities in the
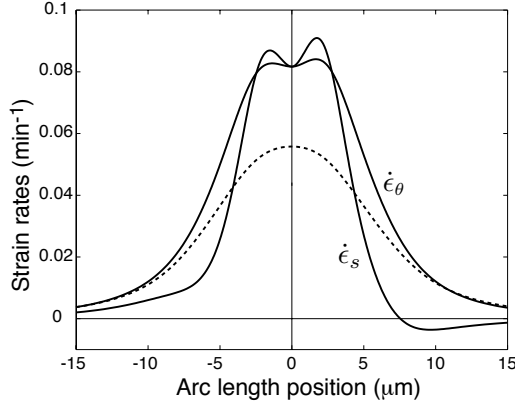
Figure 4. Strain rate profile for the cell shown in Figure 3. A slight meridional anisotropy ($\dot{\epsilon}_s > \dot{\epsilon}_\theta$) near the pole is followed by long shoulders of circumferential anisotropy ($\dot{\epsilon}_\theta > \dot{\epsilon}_s$). For comparison, the isotropic strain solution for the same geometry is shown (dotted line). Modified from [Dumais et al. 2004].

kinematics of these cells to some broadly shared processes. Therefore, the first question to ask is whether the observed strain rate profile is a geometrical requirement for all tip-growing cells. Although geometry certainly constrains kinematics, the statement above cannot be generally true since there is an infinite number of strain rate profiles that are compatible with the geometry of the system.

A comparison with the profile corresponding to an isotropic deformation of the surface reveals what is unique about the observed strain rate pattern. Setting the two equations in (1) equal to one another leads to the differential equation

$$\frac{1}{v}\frac{dv}{ds} = \frac{1}{r}\frac{dr}{ds},$$

which has as a general solution $v(s) = \frac{v_c}{r_c}r(s)$, where v_c is the tip velocity and r_c is the radius of the cylindrical region of the cell. The isotropic strain rates associated with this velocity profile are: $\dot{\epsilon}^i = \dot{\epsilon}_s = \dot{\epsilon}_\theta = \frac{v_c}{r_c}\frac{dr}{ds}$. The solution is shown in Figure 4 alongside the measured strain rates. Strain isotropy, in itself, is not a good model for the observed strain rates. However, three kinematic constraints can help explain some of the features of the observed strain rates:

(i) rotational symmetry requires that $\dot{\epsilon}_s(0) = \dot{\epsilon}_\theta(0)$;

(ii) the area under the $\dot{\epsilon}_s$ curve and the isotropic strain rate solution must be equal since it is set by the velocity of the tip, i.e. $\int_0^\infty \dot{\epsilon}_s ds = \int_0^\infty \dot{\epsilon}^i ds = v_c$;

(iii) the circumferential strain rate is asymptotic to the isotropic solution near the base of the dome, i.e.,

$$\dot{\epsilon}_\theta = \frac{v}{r}\frac{dr}{ds} \simeq \frac{v_c}{r_c}\frac{dr}{ds} = \dot{\epsilon}^i, \quad \text{for } r \to r_c.$$

Given these constraints, the main differences between the observed strain rates and the isotropic solution can be encapsulated into one observation: tip-growing cells show relatively more surface expansion near the pole than what is predicted by the isotropic solution. Since $\dot{\epsilon}_s$ exceeds $\dot{\epsilon}^i$ near the pole, it must drop below $\dot{\epsilon}^i$ away from the pole so that the second constraint is fulfilled. This feature explains the sharp

decline in $\dot\epsilon_s$ observed in Figure 4. The circumferential anisotropy is also predicted since while $\dot\epsilon_s < \dot\epsilon^i$ on the flanks of the tip, the third constraint requires that $\dot\epsilon_\theta \to \dot\epsilon^i$ at that location. Therefore, high strain rate (relative to the isotropic solution) near the pole of the cell implies circumferential anisotropy on the flanks of the dome. A similar argument was made by Green and King [1966], who demonstrated the validity of their result using locally reinforced rubber membranes. These statements will be made more precise when we discuss our model in Section 4, but first we look at the kinematics of rubber balloons from which the model was inspired.

3. Analysis of rubber balloon expansion

D'Arcy W. Thompson [1942] is widely credited for popularizing the idea that many seemingly complex biological phenomena, including cell morphogenesis, are governed by simple geometrical and physical principles. It is in this spirit that Hejnowicz et al. [1977] drew a parallel between tip growth morphogenesis and the growth of cylindrical rubber balloons. These balloons undergo an instability [Chater and Hutchinson 1984] whereby two cylindrical solutions can coexist at the given internal pressure, as shown in Figure 5. Inflation of the balloon pushes forward the zone of transition between these two cylindrical solutions. According to Hejnowicz and coworkers, the migration of the front is analogous to tip growth. The small-radius tail that precedes the front is regarded as a source of new material on which the large-radius solution feeds during growth. The narrow tail could well be pushed inside the inflating balloon to become an "internal" source of material as in tip growth. An analysis of the deformation process in rubber balloons shows that the parallels go beyond the simple geometrical analogy.

3.1. *Experimental setup.* We used an experimental configuration similar to that of Kyriakides and Chang [1991] to follow the steady-state growth of cylindrical rubber balloons (Qualatex 160Q) under constant

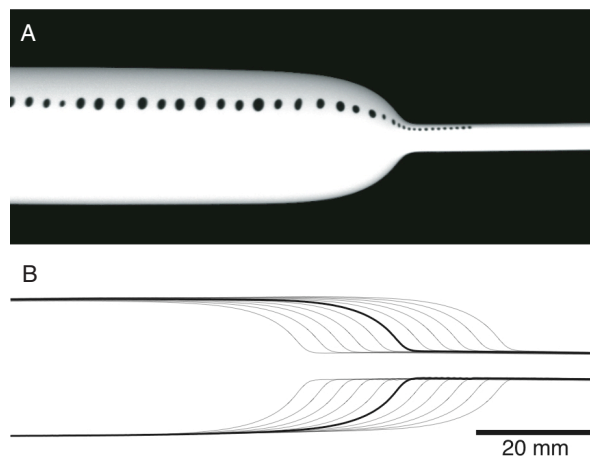**Figure 5.** (A) Snapshot of the inflated balloon with its fiducial points. (B) Propagation of the growth front during inflation. The velocity of the material entering the front is $V = 2.55$ mm/s assuming that the front is fixed in space. The velocity of the material that exits the front is $v_c = \lambda_s^{\max} V = 3.74 \times 2.55$ mm/s $= 9.54$ mm/sec, where $\lambda_s^{\max}$ is the maximal meridional stretch.
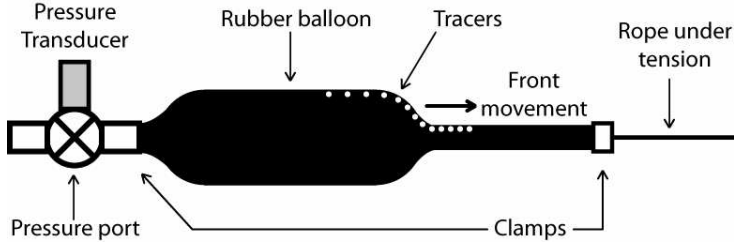
Figure 6. Diagram of the experimental setup for the rubber balloon deformation under constant internal pressure.

internal pressure P of 24.3 kPa, measured with an OMEGA PX26-005GV pressure transducer (Figure 6). To get a uniform and straight advance of the growth front, the balloon was maintained under slight axial tension by pulling with a mass $M \simeq 20$ g. The axial stress in the elastic membrane associated with this tension was approximately 50 kPa, which is negligible compared to the membrane stresses imposed by the internal pressure (210 kPa $<$ Pr/h $<$ 21 MPa). Time-lapse sequences were recorded at 10 frames per second with a PIXELINK PL-A781 camera. The meridional curvature was measured using the outline of the balloon and the stretches were computed by tracking the position of fiducial points applied to one side of the balloon (Figure 5). All further analyses were done in Matlab 7.3 and assumed an axisymmetric geometry. These data provide the information to characterize the kinematics of the balloon.

3.2. Kinematics. As the rubber balloon deforms under the internal pressure, the growth front pushes forward, delimiting two cylindrical regions in which the radii of the balloon are $r_{min} = 2.32$ mm and $r_{max} = 11.2$ mm, respectively. The undeformed radius (i.e. at $P = 0$) is $R = 2.12$ mm. The separation of the fiducial points was on average $dS \simeq 1$ mm before stretching and reached a maximum of 3.7 mm in the deformed region. The undeformed thickness of the membrane was $H = 0.27$ mm.

The kinematics of the balloon is formulated in terms of stretches. The meridional, circumferential and normal stretches are ratios of length elements before and after the deformation:

$$\lambda_s = ds/dS, \quad \lambda_\theta = r/R, \quad \lambda_n = h/H,$$

where capital letters stand for undeformed lengths. These stretches are generally not completely independent. For an incompressible material, we have $\lambda_s \lambda_\theta \lambda_n = 1$ or, alternatively, $\lambda_n = (\lambda_\theta \lambda_s)^{-1}$.

The meridional curvature is $\kappa_s = d\varphi/ds$, where φ is the angle between the normal to the surface and the axis of the balloon (Figure 2). The meridional curvature defines two regions (Figure 7A). A core region within 7 mm of the axis shows negative curvature. It corresponds to the source of material for the advance of the front. An outer region extends from a distance of 7 mm onwards. In our analogy with tip growth morphogenesis, this region stands for the deforming cell surface and is thus of special interest.

Using the balloon outline and the position of fiducial points, we computed the stretches of the elastic membrane (Figure 7B). The maximal circumferential stretch is $\lambda_\theta = 5.63$ while the maximal meridional stretch is $\lambda_s = 3.74$. For comparison with tip-growing cells, we need to define strain rates for the elastic deformation of the membrane. The velocity of material points, assuming that the front is fixed in space while material flows through it, is given by $v(s) = \lambda_s(s)V$, where V is the velocity at which underformed
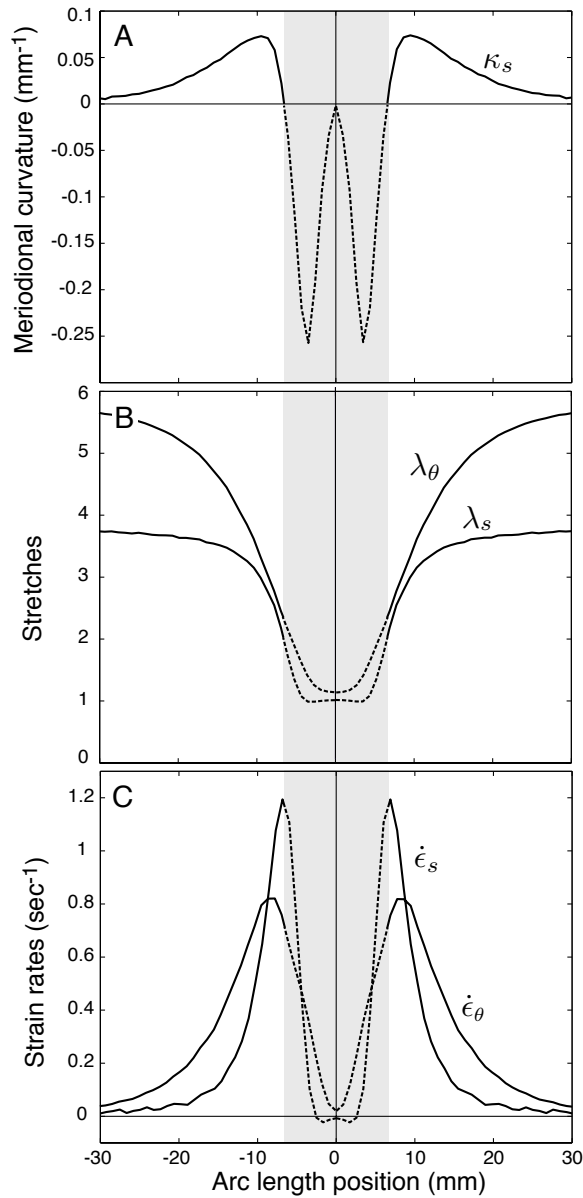
Figure 7. (A) Meridional curvature κ_s as a function of arc length s. The shaded area delimits the core region ($\kappa_s < 0$) corresponding to the "source" of material and an outer region ($\kappa_s > 0$) analogous to the dome of tip-growing cells. (B) Meridional and circumferential stretches as a function of arc length. The maximum circumferential and meridional stretches are $\lambda_\theta = 5.63$, $\lambda_s = 3.74$ respectively. (C) Meridional and circumferential strain rates as a function of arc length.

Figure 8. Three fundamental relations for thin pressurized shells.
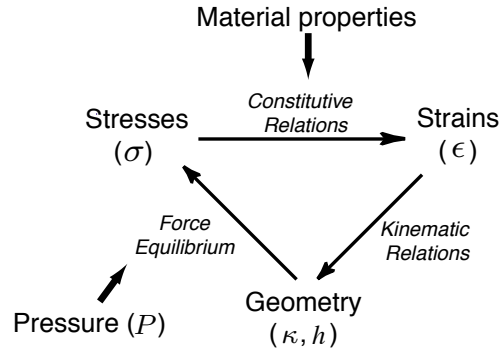
material feeds into the front. Accordingly, the strain rates are

$$\dot{\epsilon}_s = \frac{d}{ds}v = \frac{d\lambda_s}{ds}V, \qquad \dot{\epsilon}_\theta = \frac{1}{r}\frac{dr}{dt} = \frac{R}{r}\frac{d(r/R)}{ds}\frac{ds}{dS}\frac{dS}{dt} = \frac{\lambda_s}{\lambda_\theta}\frac{d\lambda_\theta}{ds}V. \tag{2}$$

The measured strain rates show substantial variation (Figure 7C). In the polar region, the two strain rates increase rapidly to a near maximal value as the material is about the exit this region. In the outer region, the strain rates decline gradually. The strain rate anisotropy first favors meridional stretching followed by long shoulders where circumferential stretching dominates. The similarities with the strain rates reported for plant cells is striking. In particular, the strain rate anisotropy and inhomogeneity follow the same trends and are mapped to the same regions in the two systems.

4. A model of tip growth

The similarities between cellular tip growth and the balloon analog prompted us to look for a simple model that could be applied to both systems. Given the sharp differences between the material properties of rubber (nonlinear elasticity) and plant cell walls (viscoplasticity), we postulate that the strain rate profile does not depend strongly on the details of the constitutive behavior. Our focus therefore is on features that are known to be shared between rubber balloons and tip-growing cells. The two systems are thin pressurized shells whose material properties are spatially varying.

The mechanics of thin shells is well understood particularly those with axisymmetric geometry [Flügge 1973]. A set of three fundamental relations connect the stresses σ, the strains ϵ, and geometrical variables such as the curvature κ of the surface and the shell thickness h; see Figure 8. The kinematic relations are already encapsulated in Equations (1) and (2). Equations are also needed for the balance of forces between the membrane stresses and the internal pressure. The wall stresses are given by

$$\sigma_s = \frac{P}{2h\kappa_\theta}, \qquad \sigma_\theta = \frac{P}{2h\kappa_\theta}\left(2 - \frac{\kappa_s}{\kappa_\theta}\right), \tag{3}$$

[Steele 2000; Dumais et al. 2006], where P is the internal hydrostatic pressure, h is the wall thickness, and κ_s and κ_θ are the meridional and circumferential curvatures. Note that the normal stress, $\sigma_n \sim P$,

is much smaller than the plane stresses, σ_s and σ_θ. We can therefore neglect the normal stress in the following treatment.

Next we must select a constitutive model to relate the strains and stresses. Several constitutive models have been suggested for the plant cell wall (see [Dumais et al. 2006], for instance) and rubber elasticity (see [Ogden 1972; Treloar et al. 1976], for example). These models are very different except in the limit of small deformation where a linear set of equations can be applied to most materials. We therefore adopt a simple linear constitutive model:

$$\begin{pmatrix} \epsilon_s(s) \\ \epsilon_\theta(s) \end{pmatrix} = \alpha(s) \begin{pmatrix} 1 & -\nu \\ -\nu & 1 \end{pmatrix} \begin{pmatrix} \sigma_s(s) \\ \sigma_\theta(s) \end{pmatrix}, \tag{4}$$

where $\alpha(s)$ is a spatially varying elastic compliance and ν is a fixed Poisson's ratio. In this model, the complexity of the material's response to stress is encapsulated in the compliance α rather than in a more complex functional form for the model. One important advantage of this model is that it can be solved analytically for a given tip geometry.

Substituting for the strains and stresses in Equation (4) yields

$$\begin{aligned} \epsilon_s &= \frac{ds}{dS} - 1 = \alpha\left(\frac{P}{2h\kappa_\theta} - \nu\frac{P}{2h\kappa_\theta}\left(2 - \frac{\kappa_s}{\kappa_\theta}\right)\right), \\ \epsilon_\theta &= \frac{r}{R} - 1 = \alpha\left(\frac{P}{2h\kappa_\theta}\left(2 - \frac{\kappa_s}{\kappa_\theta}\right) - \nu\frac{P}{2h\kappa_\theta}\right). \end{aligned} \tag{5}$$

Dividing the first equation by the second and rearranging, we get

$$ds = \left(\left(\frac{r}{R} - 1\right)\frac{(1 - 2\nu)\kappa_\theta + \nu\kappa_s}{(2 - \nu)\kappa_\theta - \kappa_s} + 1\right)dS. \tag{6}$$

Finally, dividing both sides of this equation by dt, we get

$$v(s) = \left(\left(\frac{r}{R} - 1\right)\frac{(1 - 2\nu)\kappa_\theta + \nu\kappa_s}{(2 - \nu)\kappa_\theta - \kappa_s} + 1\right)V = \lambda_s V = \frac{\lambda_s}{\lambda_s^{\max}}v_c. \tag{7}$$

From (7) it is possible to determine the velocity profile based solely on the shell geometry ($r(s)$ or $\kappa_s(s)$) and two parameters, the Poisson's ratio (ν) and a characteristic velocity (V or v_c). v_c is the velocity of the front with respect to the deformed region. We adopt this parameter since it has a natural parallel with the velocity for tip growth. The Poisson's ratio of rubber is close to 0.5 for small deformations but for strains above one it quickly drops to 0.3 [Vincent 1990]. Since the balloon strains go beyond a value of 4, we use $\nu = 0.3$.

Using the values for ν and v_c in (7) and substituting into (2) allows us to predict the strain rates for the balloon (Figure 9A). A comparison with the measured strain rates (Figure 7C) reveals that the model is surprisingly accurate despite its simplicity. In particular, the model captures the switch in strain rate anisotropy as well as the magnitude of the maximal strain rates.

The constitutive model can be modified easily to account for tip growth. Since the wall material deforms irreversibly, we must now relate stresses with strain rates rather than strains. Equations (5) then
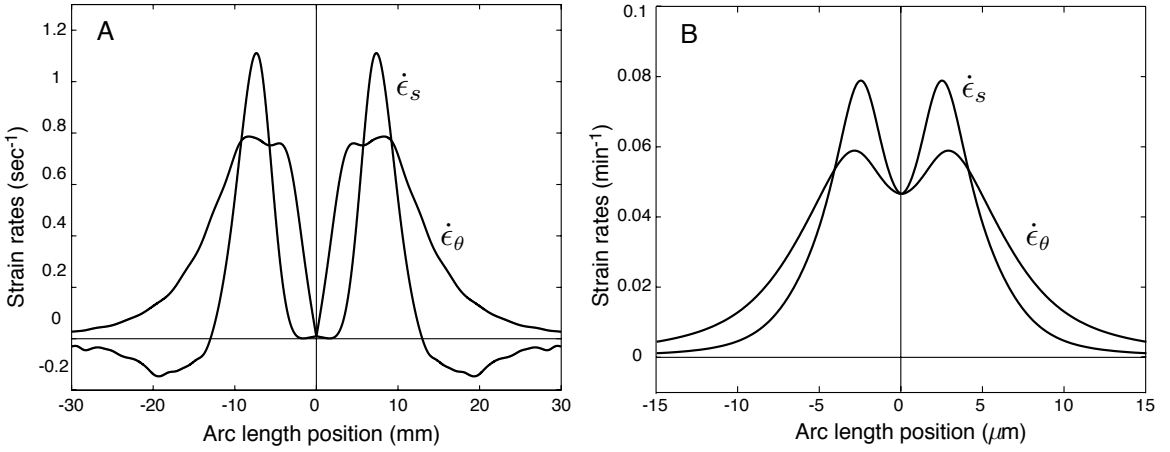
Figure 9. Predicted strain rates for the rubber balloon (A) and root hair (B) using the isotropic model.

become

$$\dot{\epsilon}_s = \frac{dv}{ds} = \alpha \left(\frac{P}{2h\kappa_\theta} - v\frac{P}{2h\kappa_\theta} \left(2 - \frac{\kappa_s}{\kappa_\theta} \right) \right), \tag{8}$$

$$\dot{\epsilon}_\theta = \frac{1}{r}\frac{dr}{ds}v = \alpha \left(\frac{P}{2h\kappa_\theta} \left(2 - \frac{\kappa_s}{\kappa_\theta} \right) - v\frac{P}{2h\kappa_\theta} \right). \tag{9}$$

Here α can be interpreted as an extensibility (inverse viscosity). Dividing the first equation by the second and rearranging gives

$$\frac{1}{v}\frac{dv}{ds} = \frac{1}{r}\frac{dr}{ds}\frac{(1-2v)\kappa_\theta + v\kappa_s}{(2-v)\kappa_\theta - \kappa_s} \tag{10}$$

This differential equation for v, with boundary condition $v(0) = 0$, has for solution

$$v(s) = \gamma r(s) \exp\left(\int_0^s G(s)\,ds\right), \qquad G(s) = \frac{1}{r}\frac{dr}{ds}\frac{(1+v)(\kappa_s - \kappa_\theta)}{(2-v)\kappa_\theta - \kappa_s}, \tag{11}$$

where γ is a constant set by the geometry and elongation rate of the tip. We used this equation and $v = 0.3$ to predict the strain rates for tip growth (Figure 9B). Again, the predicted strain rates are very similar to the observed strain rates (Figure 4). It is surprising that a model that does not include material anisotropy can nonetheless account for strain rate anisotropy so accurately. We must conclude that the observed anisotropy in the strain rates results from a similar anisotropy in the membrane stresses.

Finally, we computed the material property $\alpha(s)$ predicted by the model (Figure 10). This parameter represents a compliance for the rubber material or an extensibility for the cell wall. Given the simplicity of the model, it is unlikely that α represents a true material property. We interpret it more generally as the responsiveness of the system to the internal pressure. The parameter α maps out the polar zone that serves as a source of material ($d\alpha/ds > 0$) and the flanks of the tip, where the material is actively stretched and therefore stiffening ($d\alpha/ds < 0$). The similarity between the balloon analog and tip-growing cells is again quite remarkable.
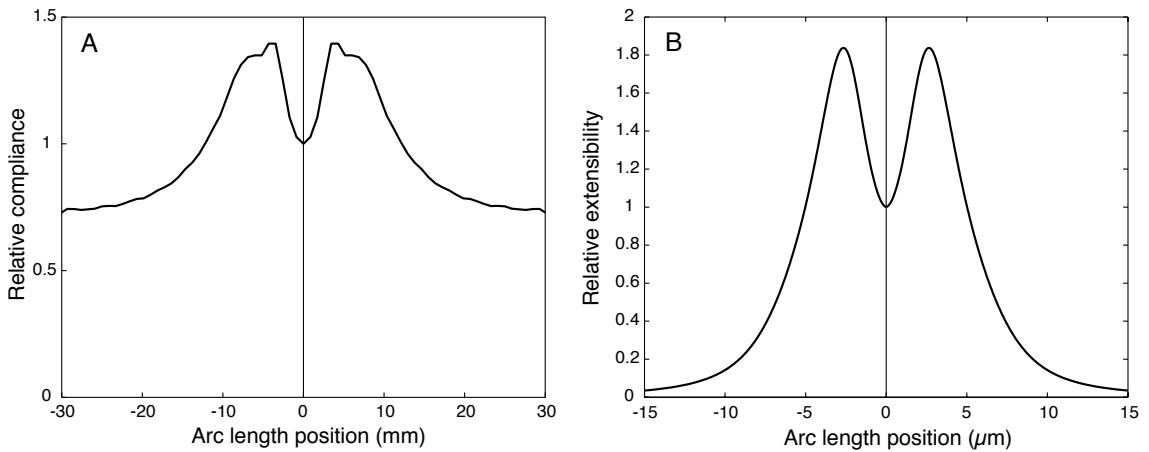
Figure 10. Predicted compliance for the rubber balloon (A) and extensibility for the root hair (B). Compliance and extensibility were normalized with respect to the value at the pole.

5. Conclusions

The similar pattern of surface expansion in tip-growing cells and rubber balloons calls for an explanation. The first explanation to consider is whether there is only a limited set of strain patterns that can maintain tip growth; that is, shared kinematics constraints could explain the similarities. As indicated above, and illustrated in Figure 4, very different strain patterns are compatible with a given tip geometry and elongation velocity. Therefore, kinematics alone is not a sufficient explanation for the similar expansion pattern. Tip-growing cells and rubber balloons must share features at a more fundamental level. We propose that the presence of a source of soft material in the polar region is one likely common feature. In the balloon, the rapid stiffening of the material as it is stretched can explain the characteristic geometry of the growing front. Strain stiffening has also been proposed for tip growth morphogenesis [Green and King 1966]. The stiff cellulose microfibrils that make up a large volume fraction of plant cell walls are synthesized in the polar region presumably in a relaxed state. As the tip surface deforms, the fibrils would be progressively put under tension thus increasing rapidly the stiffness of the wall. Clearly, plant cell expansion is *not* an elastic phenomenon but the presence of long cellulose microfibrils in the wall means that the cell possesses some memory of past deformation.

The main conclusion of this work is that many aspects of cell morphogenesis, despite their complex biological underpinning, may still be explained via relatively simple physical principles. For the case of tip growth morphogenesis, we have shown that a simple constitutive model with isotropic material properties is sufficient to explain the observed strain rate anisotropy. We postulate that strain stiffening of the wall's molecular fabric accounts for the meridional variation of the wall extensibility.

References

[Castle 1958] E. S. Castle, "The topography of tip growth in a plant cell", *J. Gen. Physiol.* **41**:5 (1958), 913–926.

[Chater and Hutchinson 1984] E. Chater and J. W. Hutchinson, "On the propagation of bulges and buckles", *J. Appl. Mech.* (*Trans. ASME*) **51** (1984), 269–277.

[Chen 1973] J. C. W. Chen, "The kinetics of tip growth in the *Nitella* rhizoid", *Plant Cell Physiol.* **14**:4 (1973), 631–640.

[Dumais et al. 2004] J. Dumais, S. R. Long, and S. L. Shaw, "The mechanics of surface expansion anisotropy in *Medicago truncatula* root hairs", *Plant Physiol.* **136** (2004), 3266–3275.

[Dumais et al. 2006] J. Dumais, S. L. Shaw, C. R. Steele, S. R. Long, and P. M. Ray, "An anisotropic-viscoplastic model of plant cell morphogenesis by tip growth", *Int. J. Dev. Biol.* **50** (2006), 209–222.

[Flügge 1973] W. Flügge, *Stresses in shells*, 2nd ed., Springer, Berlin, 1973.

[Green and King 1966] P. B. Green and A. King, "A mechanism for the origin of specifically oriented textures in development with special reference to *Nitella* wall texture", *Aust. J. Biol. Sci.* **19** (1966), 421–437.

[Harold 1990] F. M. Harold, "To shape a cell: an inquiry into the causes of morphogenesis of microorganisms", *Microbiol. Rev.* **54**:4 (1990), 381–431.

[Hejnowicz et al. 1977] Z. Hejnowicz, B. Heinemann, and A. Sievers, "Tip growth: Patterns of growth rate and stress in the *Chara* rhizoid", *Zeitung der Pflanzenphysiologie* **81** (1977), 409–424.

[Kyriakides and Chang 1991] S. Kyriakides and Y. C. Chang, "The initiation and propagation of a localized instability in an inflated elastic tube", *Int. J. Solids Struct.* **27**:9 (1991), 1085–1111.

[Ogden 1972] R. W. Ogden, "Large deformation isotropic elasticity: on the correlation of theory and experiment for incompressible rubberlike solids", *P. Roy. Soc. Lond. A Mat.* **326**:1567 (1972), 565–584.

[Reinhardt 1892] M. O. Reinhardt, "Das Wachsthum der Pilzhyphen", *Jahrbücher für wissenschaftliche Botanik* **23** (1892), 479–566.

[Shaw et al. 2000] S. L. Shaw, J. Dumais, and S. R. Long, "Cell surface expansion in polarly growing root hairs of *Medicago truncatula*", *Plant Physiol.* **124** (2000), 959–970.

[Steele 2000] C. R. Steele, "Shell stability related to pattern formation in plants", *J. Appl. Mech.*(*Trans. ASME*) **67**:2 (2000), 237–247.

[Thompson 1942] D. W. Thompson, *On growth and form*, 2nd ed., Cambridge Univ. Press, Cambridge, 1942. Reprinted by Dover, New York, 1992.

[Treloar et al. 1976] L. R. G. Treloar, H. G. Hopkins, R. S. Rivlin, and J. M. Ball, "The mechanics of rubber elasticity", *P. Roy. Soc. Lond. A Mat.* **351**:1666 (1976), 301–330.

[Vincent 1990] J. F. V. Vincent, *Structural biomaterials*, Princeton University Press, Princeton, 1990.

[Vogel 2003] S. Vogel, *Comparative biomechanics: life's physical world*, Princeton University Press, Princeton, 2003.

ROBERTO BERNAL: rbernal@oeb.harvard.edu
Department of Organismic and Evolutionary Biology, Harvard University, 16 Divinity Ave., Cambridge, MA 02138, United States

ENRIQUE R. ROJAS: errojas@fas.harvard.edu
Department of Physics, Harvard University, 17 Oxford St., Cambridge, MA 02138, United States

JACQUES DUMAIS: jdumais@oeb.harvard.edu
Department of Organismic and Evolutionary Biology, Harvard University, 16 Divinity Ave., Cambridge, MA 02138, United States